(Received 23 September 2025, Accepted 13 November 2025, Scheduled 22 November 2025)

Wideband Low RCS Metasurface Conformal Sheet for Stealth Applications

Shimaa A. M. Soliman*, Sherine I. A. El-Rahman, and Hany M. Zamel

Microwave Engineering Department, Electronics Research Institute (ERI), Cairo, Egypt

ABSTRACT: In this paper, a wideband design of a conformal metasurface for RCS reduction in the range of 6.3∼8.3 GHz is introduced. The proposed unit cell has a reflection amplitude less than −0.5 dB. The methodology for reducing the radar cross section using metamaterial is introduced along with the evolution of the design of the proposed unit cell. The conformal array is modeled using this unit, and the performance of a metasurface when being attached to a conformal metallic object is investigated. When the proposed metasurface is attached to a 3D object, it can achieve more diffused scattering patterns and wide scattering angles, regardless of the polarization of the incident waves and across a wide range of incident angles. It can achieve more than 10 dB reduction RCS. The sheet operates well for incident wave angles up to 60°. Both simulated and measured results demonstrate that the conformal metasurface effectively achieves diffuse reflection and RCS reduction which holds significant potential for applications in the field of advanced stealth technology, and the sheet size is scalable to larger sizes.

1. INTRODUCTION

Radar cross section (RCS) reduction is a key requirement in stealth technology for metallic platforms used in defense, aerospace, and communication systems. Metasurfaces have emerged as an effective approach for suppressing backscattered energy from both planar and conformal structures. Different methods are used for reducing RCS, such as frequency selective surfaces (FSSs) [1], artificial magnetic conductor (AMC) [2], electromagnetic band-gap (EBG) structures [3], electromagnetic cloaking [4], orbital angular momentum [5], anomalous reflection metasurfaces [6–8], and metamaterial [9, 10].

In recent years, metasurfaces, which act as two-dimensional analogs of metamaterials, have gained widespread use in improving the efficiency and performance of antennas and wireless systems. They offer the distinct capability to precisely control the phase, amplitude, and polarization of incident electromagnetic waves, while also providing advantages like ease of fabrication and compact size [11–14]. Rangula et al. presented a chessboard metasurface composed of unit cells, achieving significant backscattering reduction across the 10–38 GHz frequency range for incident waves polarized in both the X and Y directions [15]. Wang et al. proposed a prismatic conformal metasurface designed for wideband RCS utilizing optimized multi-element phase cancellation [16]. Chatterjee et al. presented an ultrathin metasurface for polarization conversion, effectively achieving RCS reduction on both planar and conformal surfaces. A polarization converter is designed using a modified concentric double square ring resonator unit cell, featuring an air gap between the substrate and ground plane [17]. Tiwari et al. designed and characterized a broadband, polarization-insensitive metasurface absorber for RCS reduction [18]. The structure consists of resistor-loaded metallic patches patterned on an FR-4 dielectric substrate, with a metallic ground plate separated by an air spacer. Recently, Khan et al. presented a conformal metasurface absorber designed using indium tin oxide (ITO), polyethylene terephthalate (PET), and polyvinyl chloride (PVC). The proposed structure exhibits ultra-wideband absorption, angular stability, and unique flexibility and optical transparency, making it suitable for advanced stealth and electromagnetic compatibility applications [19].

This paper introduces a novel wideband design for a conformal metasurface aimed at reducing RCS in the frequency range of 6.3 to 8.3 GHz. The proposed metasurface utilizes passive unit cells, which are specifically engineered to be attached to conformal 3D metallic objects. Simulated and experimental results show that this design achieves significant RCS reduction, with improvements greater than 10 dB across a wide range of incident angles (0° to 60°) and polarization states. The metasurface produces diffuse scattering patterns, ensuring enhanced stealth performance in real-world applications. This research contributes to the advancement of stealth technology, presenting a viable solution for RCS reduction in complex, curved geometries, which holds great potential for future defense and aerospace technologies.

2. METHODOLOGY FOR REDUCING THE RADAR CROSS SECTION USING METAMATERIAL

Metasurfaces with phase gradients enable accurate manipulation of wave propagation by creating sharp phase discontinuities across their surface. They were initially developed to generate spiral waves, demonstrating their capability to manipulate light [20]. The presence of phase discontinuities on the surface of the metasurface invalidates the classical Snell's Law, which assumes that the angle of incidence equals the angle of reflection for plane waves interacting with isotropic surfaces. In-

* Corresponding author: Shimaa A. M. Soliman (shimaa_megahed@eri.sci.eg).

stead, the incident wave can either couple into a surface wave or undergo anomalous reflection. This property makes metasurfaces with phase gradients a promising material for RCS reduction applications [12, 21]. Numerous configurations have been proposed to either couple incident waves into surface modes or induce anomalous reflection behaviors [22–25]. The phase gradients $d\Phi_x$ and $d\Phi_y$ represent the gradients along x and y axes, respectively, with their resultant vector denoted as $d\Phi_r$, as illustrates in Fig. 1. The incident, reflected, and coupling wave vectors are denoted by (K_i), (K_r), and (K_c).

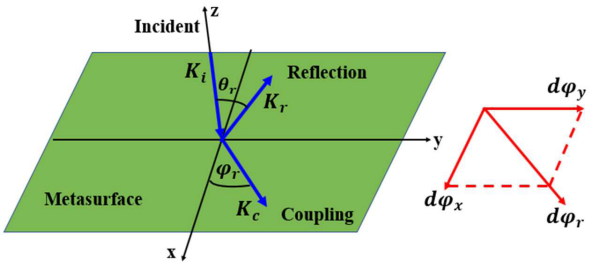

FIGURE 1. Schematic illustration of the phase-gradient metasurface.

Illumination of the phase-gradient metasurface by a propagating wave can lead to one of two effects: the wave may be reflected in an anomalous direction, or it may couple into a guided surface mode. The interaction between the incident wave vectors (K_i) and $d\Phi_r$ critically influences the resulting behavior.

The incident angle (θ_i) and reflected angle (θ_r) are related by [26]:

$$K_r \sin(\theta_r) - K_i \sin(\theta_i) = d\phi_x \quad (1)$$

$$K_r \cos(\theta_r) \sin(\theta_r) = d\phi_y \quad (2)$$

Anomalous reflection and surface wave coupling can reduce specular reflection when the phase-gradient metasurface is illuminated by a normally incident wave. Since the phase-gradient metasurface is composed of unit cells with varying reflection phases, its overall phase gradient is defined by the phase differences between adjacent unit cells. If these phase differences remain consistent over a broad frequency range, the resulting phase gradient can be considered constant across a wide bandwidth. Consequently, the phase-gradient metasurface can maintain its ability to anomalously reflect incident waves or couple them into surface waves over this broad frequency range. Based on these principles, wideband RCS reduction can be effectively achieved using the phase-gradient metasurface [12, 21].

A phase variation of 2π per period is selected to enable convenient periodic arrangement along the x- or y-axis of the phase-gradient metasurface. To achieve the required phase gradient, a unit cell of metasurface (MS) is designed to allow two distinct resonances to occur. The frequency range of the low RCS and wave cancellation would be the difference between these two resonances. The reflected phase is estimated under open boundary conditions, and the plane wave is set as normal incidence. Fig. 2 shows two reflection phases in x and y with two resonances of zero reflection phase occurring at F_1 and F_2, respectively. However, the reflection phase difference between the two zero reflection phases is 360° as shown in the

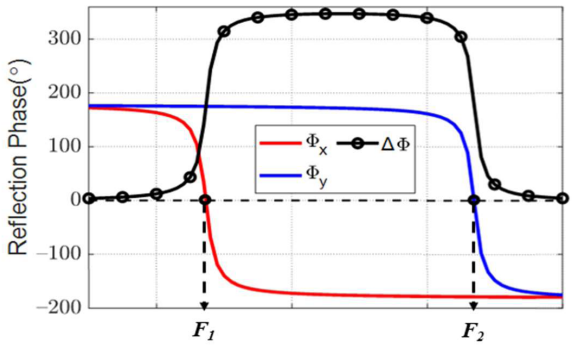

FIGURE 2. Variation of the reflection phase in x and y directions and the corresponding phase difference.

figure. As noticed, the sharp slope of the phase variation with frequency can significantly affect the phase difference, and in order to achieve the desired difference, this slope should be slowed down.

3. EVOLUTION OF THE RCS REDUCTION UNIT CELL DESIGN

The proposed MS cell structure is depicted in Fig. 3. This unit comprises one layer of grounded dielectric substrate. The substrate is 1.575 mm thick, of ROGERS 5880 (dielectric constant 2.2, loss tangent 0.007). The model is started with a metallic rectangular shape with length 13.4 mm and width 14 mm in order to create two nonidentical resonances.

By studying the effect of the thickness of the substrate as shown in Fig. 4, increasing the thickness can positively affect the phase delay by increasing the time, the wave spends inside the substrate material before reflecting back into the air. Based on this parametric study and to achieve the required phase slope, a substrate with thickness $h = 1.575$ mm is chosen. Fig. 5

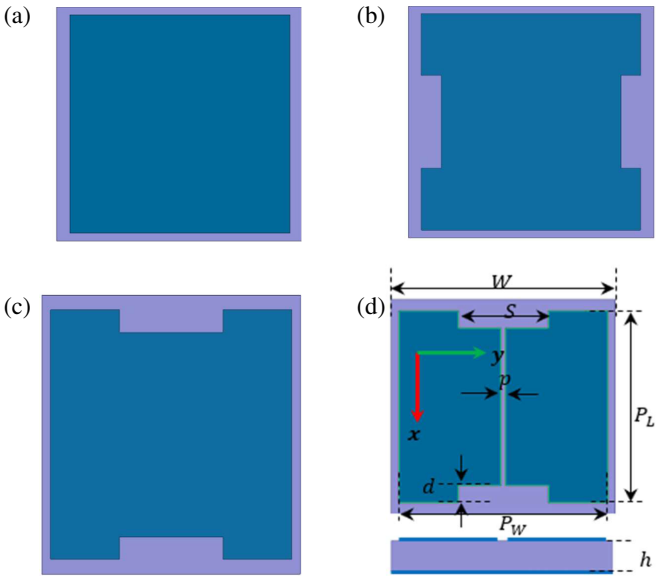

FIGURE 3. Evolution of the metasurface unit cell design: (a) Initial model (Model 1), (b) Modified model (Model 2), (c) Modified model (Model 3), and (d) Finalized design (Model 4), with dimensions (in mm).

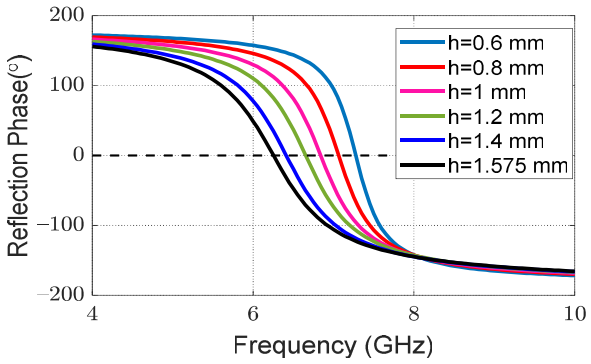

FIGURE 4. The reflection phase vs frequency at different substrate thickness (h).

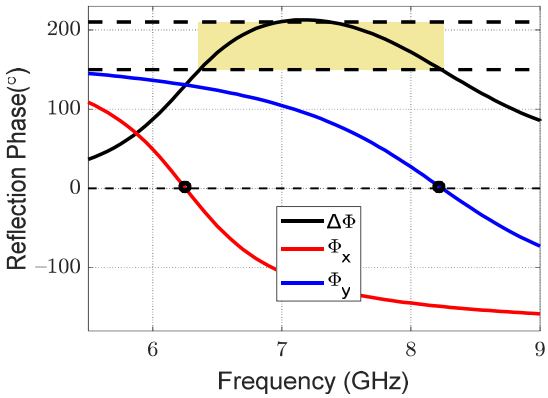

FIGURE 5. Variation of the slow reflection phase in x and y directions and the corresponding achieved phase difference of $\approx 180°$.

shows an example of a slow reflection phase in x and y directions resonating at two different frequencies, resulting in phase difference of $\approx 180°$.

Table 1 presents the dimensions of the design. The unit structure is modeled in Ansys HFSS and inserted in boundary condition in order to estimate the reflected magnitude and phase as shown in Fig. 6. Fig. 3(a) and Fig. 7(a) show the initial model and the corresponding reflection in x and y directions along with the phase difference which does not satisfy the required condition for wave cancellation as the two zero reflection phases are so close. Two notches are made along the borders, at the opposite edges as shown in Fig. 3(b), which enhances the phase difference range with a certain limit as shown un Fig. 7(b). The corresponding achieved phase difference is nearly $180°$ but in a narrow frequency range. In order to widen the range or the RCS reduction, the unit cell is rotated to switch between the x and y reflections. The refection phase response

TABLE 1. Dimension of the proposed unit cell.

Parameters	Values	Parameters	Values
P_L	13.4 mm	h	1.575 mm
P_W	14 mm	p	0.3mm
W	15 mm	d	1.2 mm
S	6 mm		

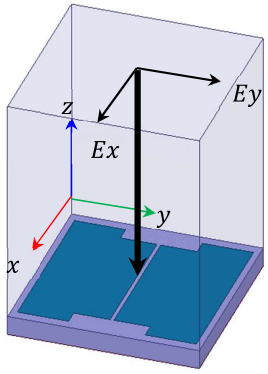

FIGURE 6. The unit cell inside in boundary conditions.

in the x-direction is slower than in the y-direction; therefore, it is kept fixed at the desired frequency of 6.3 GHz. The orthogonal reflection is then manipulated by creating a cut in the middle of the design, which forces the y-component to shift to a higher frequency. The two design steps and corresponding reflection phases are shown in Figs. 3(c), 3(d) and Figs. 7(c), 7(d). The final MS cell design is a simple slotted square patch with edge notches, to achieve a $180° \pm 30°$ phase shift across a broad frequency range. The reflection phase and reflection amplitude of the unit are shown in Fig. 8. The unit achieves a reflection phase difference of $180° \pm 30°$ from 6.3 GHz to 8.3 GHz. Fig. 9 shows the Z parameter, clearly illustrating the two non-identically spaced resonances overlapping at 50 Ω.

To further investigate the tunability of the proposed metasurface unit, a comprehensive parametric study was conducted on three key geometrical parameters: slot spacing s, periodicity p, and slot width d. The reflection phase response was evaluated for each parameter while keeping all other dimensions fixed. The objective of this analysis is to identify the dominant parameter influencing the phase difference and to determine the required geometrical range that satisfies the average phase difference of approximately $180°$, which is essential for achieving efficient wave cancellation. Fig. 10 shows the reflection phase variation as a function of frequency for different values of s ranging from 2 mm to 8 mm. It is observed that parameter s has the strongest influence on the phase response, where increasing s yields a noticeable shift in the reflection phase curve either above or below the target phase level. In particular, decreasing s shifts the phase response upward, whereas increasing s drives the phase response downward. This monotonic behavior enables the tuning of the phase difference around the desired average value of $180°$. The slot width p also has a significant effect on the phase difference as can be noticed from Fig. 11. The presented results show different variations of the phase difference for p ranging rom 0.1 mm to 0.5 mm. Finally, the notch width d mainly acts as secondary tuning factors, where it regulates the usable bandwidth and refines the smoothness of the phase transition without significantly altering its average level. Fig. 12 shows the reflection phase difference variation with frequency for different d ranging from 0.8 mm to 1.5 mm. The optimum values extracted from the parametric study are: $s = 6$ mm, $p = 0.3$ mm, and $d = 1.2$ mm.

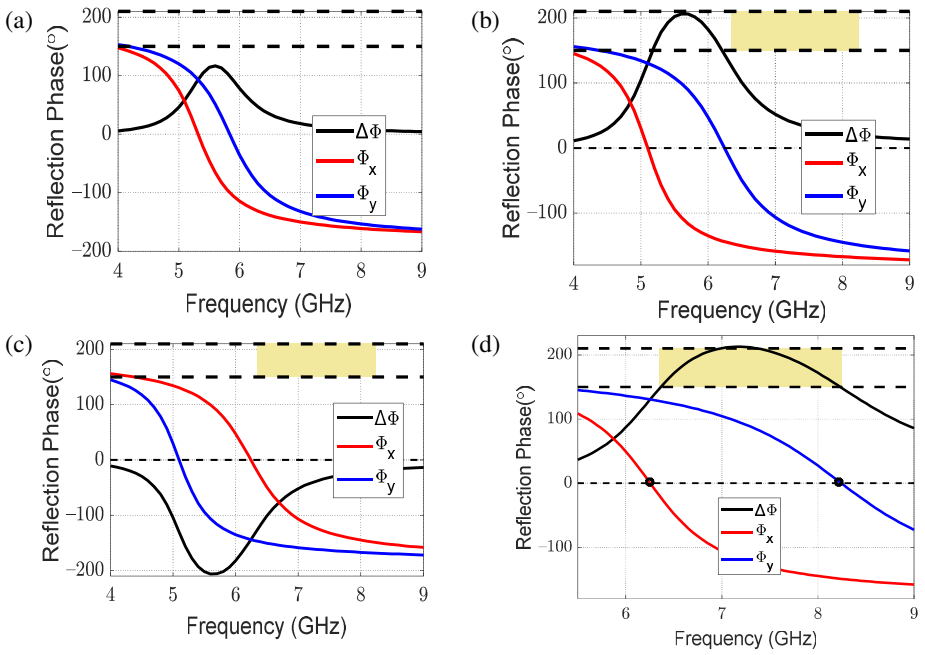

FIGURE 7. Reflection phase and phase difference for the proposed cell. (a) Model #1. (b) Model #2. (c) Model #3. and (d) Model #4.

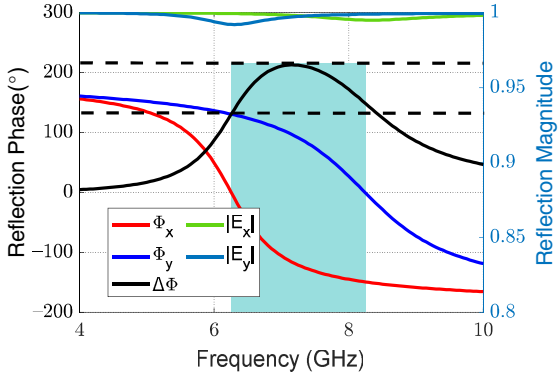

FIGURE 8. Reflection magnitude, phase, and phase difference of the final cell.

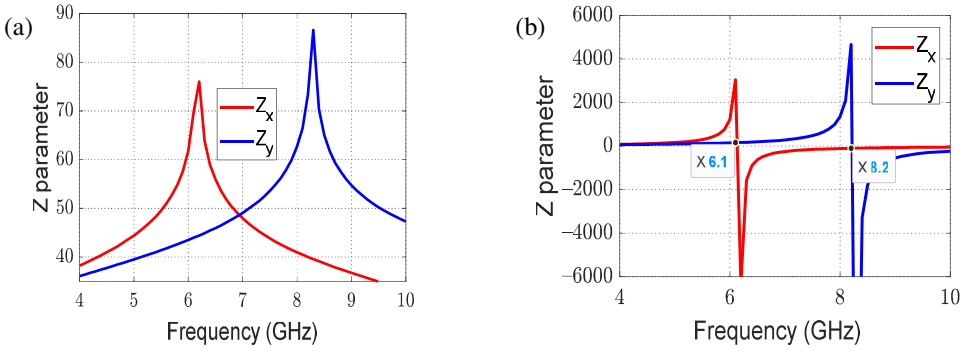

FIGURE 9. Z-parameter for the proposed unit cell. (a) Real. (b) Imaginary.

The surface current vector at different frequencies 6.5, 7, 7.5, and 8 GHz are plotted in Fig. 13. It can be concluded that the unit cell is excited at the resonance frequencies 6.5 and 8 GHz. For more investigation, the E-field distributions of the proposed unit cell at the resonances under normal incident x- and y-polarized waves are shown in Fig. 14. At the first resonance frequency 6.3 GHz, the unit cell is excited when illuminated by the x-polarized wave, as depicted in Fig. 14(a). This is evident from the concentration of the E-field at the two edges along the y-axis. Conversely, when illuminated by the y-polarized

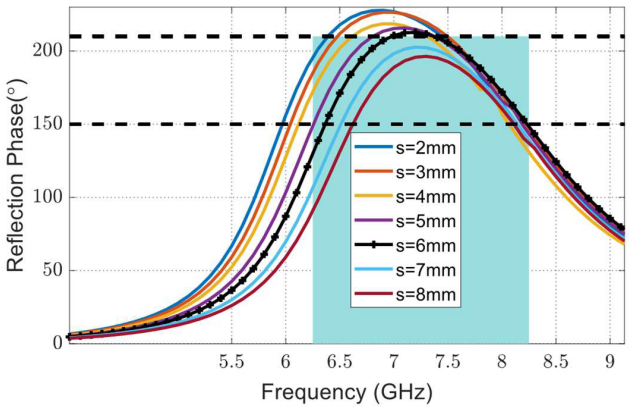

FIGURE 10. Reflection phase difference variation with frequency for different s ranging from 2 mm to 8 mm.

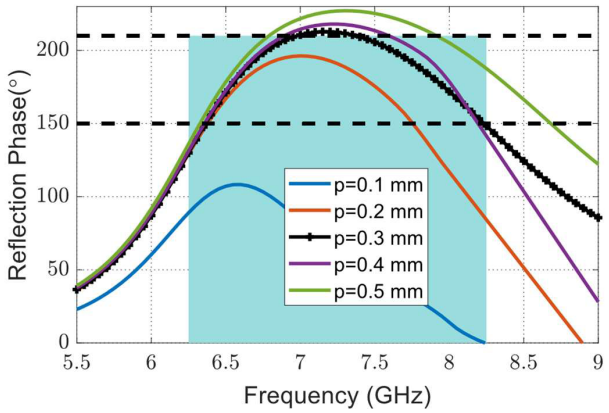

FIGURE 11. Reflection phase difference variation with frequency for different p ranging from 0.1mm to 0.5 mm.

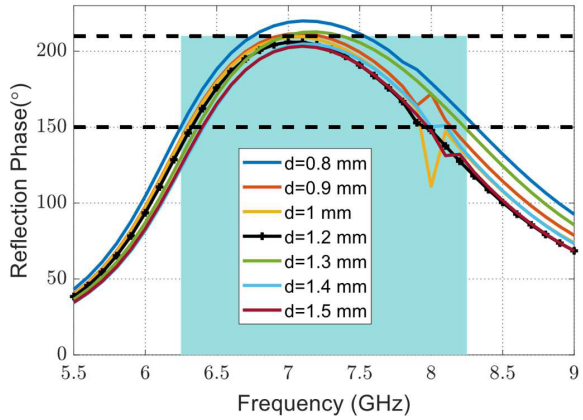

FIGURE 12. Reflection phase difference variation with frequency for different d ranging from 0.8 mm to 1.5 mm.

wave, the unit cell remains unexcited, as shown in Fig. 14(b). Contrarily, at the second resonance at 8.3 GHz, the unit cell is excited by the y-polarized wave, as seen in Fig. 14(d), while it remains unexcited when the x-polarized wave is applied, as shown in Fig. 14(c). Using the reflection magnitude and phase obtained from this unit cell, the 10 dB reduction in the RCS as a function of the frequency can be estimated using an approximate expression provided in [15]. Fig. 15, shows a significant drop in the frequency range 6.3 GHz–8.3 GHz.

4. EQUIVALENT CIRCUIT OF THE MS UNIT CELL

The equivalent circuit of the MS unit cell is derived based on the surface impedance analysis, incorporating both series and parallel configurations to model the EM response [27, 28]. The total impedance (z_{tot}), as shown in Fig. 16, is expressed as the parallel combination of surface impedance (Z_S) and ground impedance (Z_G):

$$Z_S \parallel \| Z_G \tag{3}$$

$$z_{tot} = \frac{Z_S Z_G}{Z_S + Z_G} \tag{4}$$

The reflection coefficient (Γ_G) at the ground plane interface is given by:

$$\Gamma_G = \frac{Z_G - Z_o}{Z_G Z_o} \tag{5}$$

where Z_o is the characteristic impedance of free space. The ground impedance (Z_G) can be rewritten in terms of Γ_G as:

$$Z_G = Z_o \frac{1 + \Gamma_G}{1 - \Gamma_G} \tag{6}$$

Similarly, the total reflection coefficient (Γ_{Tot}) and total impedance (Z_{tot}) are related by:

$$\Gamma_{\text{Tot}} = \frac{Z_{tot} - Z_o}{Z_{tot} Z_o} \tag{7}$$

$$Z_{tot} = Z_o \frac{1 + \Gamma_{tot}}{1 - \Gamma_{tot}} \tag{8}$$

The surface impedance (z_s) is then extracted from:

$$z_s = \frac{Z_G Z_{tot}}{Z_G - Z_{tot}} \tag{9}$$

The RLC equivalent circuit for the MS unit cell is illustrated in Fig. 17. Fig. 17 shows two configurations, the expanded LC circuit and corresponding simplified LC circuit, for two distinct configurations are provided for TE (E_y) and TM (E_x) polarizations. Circuit parameters of the expanded circuits, listed in Table 2, include capacitances and inductances, which were optimized to match the simulated and analytical phase responses.

TABLE 2. Equivalent circuit parameter.

Parameter	Values	Parameter	Values
$C1_y$	0.3181 pF	$C1_x$	0.1133 pF
$C2_y$	0.7452 pF	$C2_x$	0.1861 pF
$C3_y$	1.1524 pF	$L1_x$	0.5104 nH
$L1_y$	0.3553 nH	$L2_x$	0.7291 nH
$L2_y$	0.24871 nH		

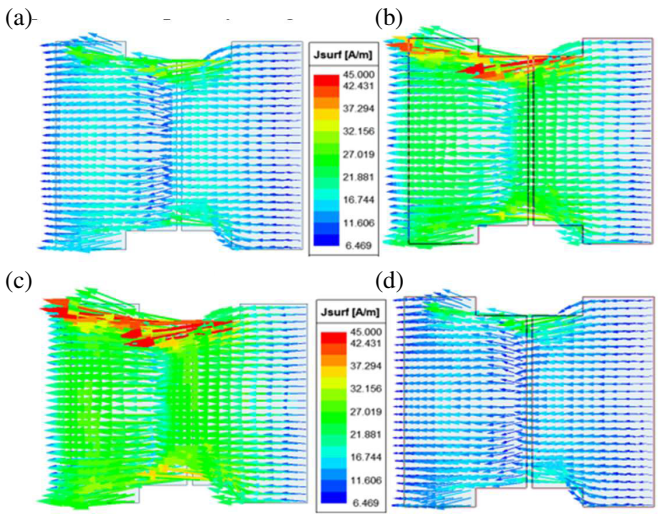

FIGURE 13. The surface current vector at multiple frequencies. (a) 6.5 GHz. (b) 7 GHz. (c) 7.5 GHz. (d) 8 GHz.

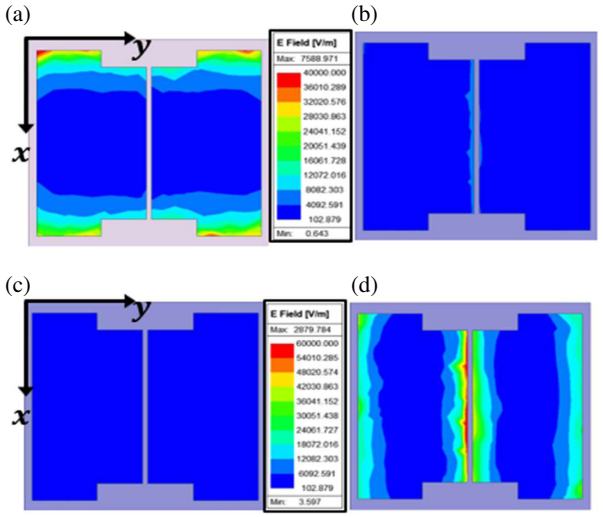

FIGURE 14. E-field distribution at the two resonances (a) 6.3 GHz for x incident waves. (b) 6.3 GHz under $x$incident waves. (c) 8.3 GHz under y incident waves. (d) 8.3 GHz under y incident waves.

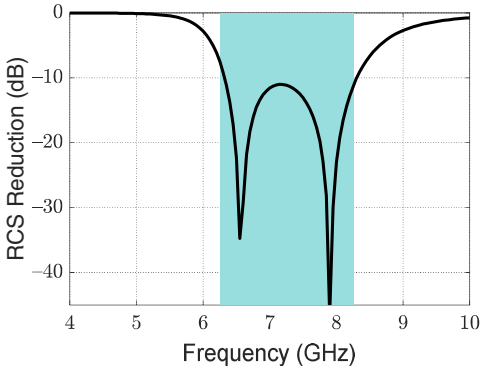

FIGURE 15. Calculated RCS using the reflection magnitude and phase for the proposed unit cell.

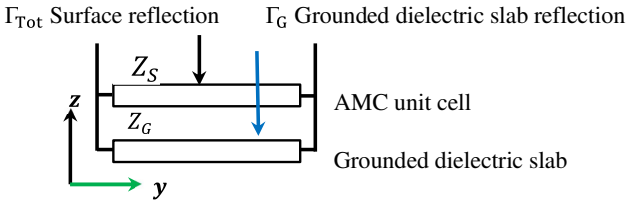

FIGURE 16. Equivalent circuit for the MS unit cell.

The equivalent parameters for the simplified circuits are listed in Table 3 and Table 4. The distinct circuit topology shown in Fig. 17(a) for Transverse Electric (TE) polarization directly models the electromagnetic behavior of the unit cell when being excited in this direction. When the incident E field is aligned with the y-axis, it induces surface currents primarily flowing along the y-direction on the metallic elements. The Inductors (L_{1y}, L_{2y}) in the equivalent circuit model the kinetic inductance that results from these currents. This inductance represents the inertia of the current flow within the metallic traces.

TABLE 3. Simplified equivalent circuit parameter.

Simplified equivalent Circuit for X-direction	
L_{eqx} (nH)	C_{eqx} (pF)
0.4557	0.2516

TABLE 4. Simplified equivalent circuit parameter.

Simplified equivalent Circuit for Y-direction	
L_{eqy} (nH)	C_{eqy} (pF)
0.2663	0.1476

As the current flows, charges accumulate at the ends of the strips or across the gaps separating adjacent metallic parts. The Capacitors (C_{2y}, C_{3y}) represent the capacitive coupling between neighboring metallic elements or the capacitance across the physical gaps within the unit cell's structure. This models the stored electric energy due to charge accumulation. The RLC equivalent circuit shown in Fig. 17(b) for the Transverse Magnetic (TM) polarization reflects a fundamentally different interaction with the unit cell's geometry compared to the TE case. When the incident E-field is aligned with the x-axis, it drives currents that are primarily in the x-direction. The unit cell's structure likely presents capacitive gaps or breaks directly in the path of the E_x field. The Capacitors (C_{1x}, C_{2x}) in the circuit primarily model this gap capacitance, representing charge accumulation across the insulating material or the free space where the E field is concentrated. While the Inductors (L_{1x}, L_{2x}) primarily model the inductance associated with the current loops that are formed as the current is shunted around the metallic patches or strips. They also account for the free-space inductance resulting from the magnetic field coupling across the unit cell.

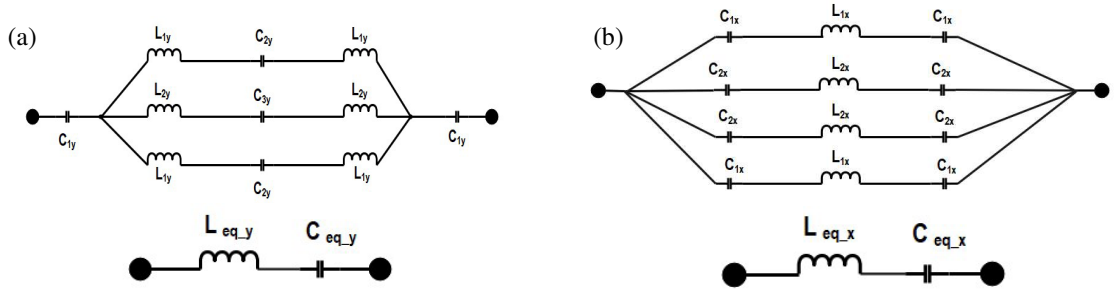

FIGURE 17. RLC equivalent circuit (a) TE (E_y), (b) TM (E_x).

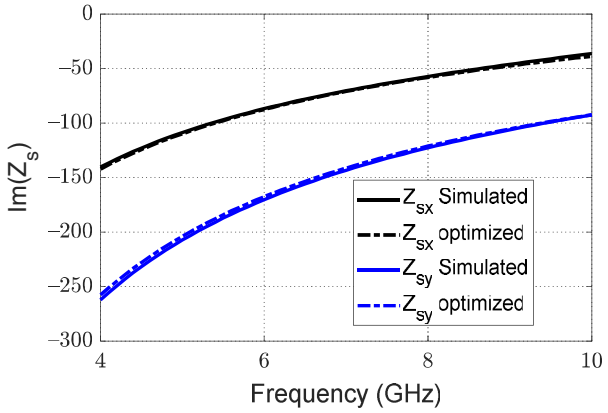

FIGURE 18. Simulated Z_s (at Normal incident) for TE (E_y) and TM (E_x).

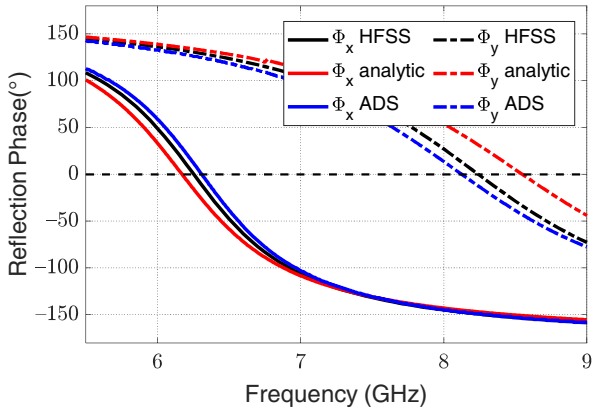

FIGURE 19. Phase variation. One figure (HFSS and Analytic).

Figure 18 presents the simulated surface impedance resulting from the HFSS (Z_S) under normal incidence for both TE and TM polarizations, matching with the achieved one with the optimized circuit parameters. Additionally, the optimized circuit parameters can be used to analytically calculate the phase response from the unit cell in order to verify the phase results achieved by the simulation. The phase variation plot presented in Fig. 19 compares results from HFSS and analytical one, demonstrating good agreement and validating the proposed equivalent circuit. These results highlight the effectiveness of the equivalent circuit model in capturing the MS unit cell's electromagnetic response, providing a useful tool for further design and optimization of such structures.

5. PROPOSED PLANNAR AND CONFORMAL METASURFACE SHEET

Utilizing the proposed metasurface unit, a planar conformal array has been designed with a cylindrical center angle of $\alpha = 400\,\text{mm}$ curvature. The elements are arranged in two-dimensional lattice sized $m \times n = 4 \times 4$. This smaller array is arranged in larger one with size $M \times N = 2 \times 2$. The larger array is arranged in a way so that the elements are rotated 90° around the center, this allows guaranteed wave cancellation in both directions. Fig. 20(a) shows a schematic of the $M \times N = 2 \times 2$ Planner, whereas Fig. 20(b) presents the simulated normalized monostatic RCS for 3 planar MS sheet compared to perfect conductor of same size, 2×2, 3×3 and 4×4 boards. To verify the efficiency of the planar metasurface in reducing RCS, we compare the bistatic RCS of the metasurface with a perfect electric conductor (PEC), as shown. It can be observed that the planar metasurface achieves an RCS reduction by more than 10 dB. Based on these results, it is noticed that the RCS reduction for a sheet with an even number of metasurface cells exhibits better results.

The planar reflecting metasurface is converted to a conformal one by bending and placing the metasurface on a cylindrical surface with a radius α. The smaller the cylinder radius is, the more conformal the surface is. Fig. 21 shows a schematic of the 4×4 chessboard conformal metasurface with bending radius $\alpha = 400\,\text{mm}$ with plot of the 3D scatted pattern at 6.5 GHz. In the case of normal incidence, $\theta_i = 0^\circ$, the monostatic scattering patterns of a planar 4×4 metasurface at 6.5 GHz are investigated and compared with a planner PEC surface of same size. As presented in Fig. 22, both cases show significant reduction in the RCS in the broad side direction, compared to the PEC surface, and the main scattered beam is suppressed. The variation of normalized monostatic RCS of the MS sheet at 6.5 GHz for multiple bending radii, compared to a PEC sheet of the same size as a reference, is presented in Fig. 23. As noticed either the planner or the curved surface significantly enhances the desired reduction in the RCS. Moreover, the 3D results of the bistatic scattered RCS of the same sheet at 6.5 GHz for multiple incidence angles, presented in Fig. 24, also show a significant re-

TABLE 5. The work previously reported in the literature.

Ref.	Unit Cell Size (λ^3)	Ms BW	Angular Stability	RCS Reduction (dB)	Measurement Type
[22]	$0.43 \times 0.43 \times 0.13$	10.2–20.7 GHz	0∼45	Planar	Monostatic
[23]	$0.39 \times 0.39 \times 0.2$	4.0–12 GHZ	0∼45	Planar	Monostatic
[24]	$0.59 \times 0.59 \times 0.17$	10.5–19.5 GHZ	0∼40	Planar and Conformal	Monostatic
[25]	$0.46 \times 0.46 \times 0.14$	8.5–17 GHZ	0∼55	Planar and Conformal	Monostatic
[26]	$0.65 \times 0.65 \times 0.13$	13-39GHZ	0∼60	Planar and Conformal	Monostatic
This work	$0.33 \times 0.31 \times 0.037$	6.3–8.3GHZ	$0 \sim 60$	Planar and Conformal	Monostatic & Bistatic

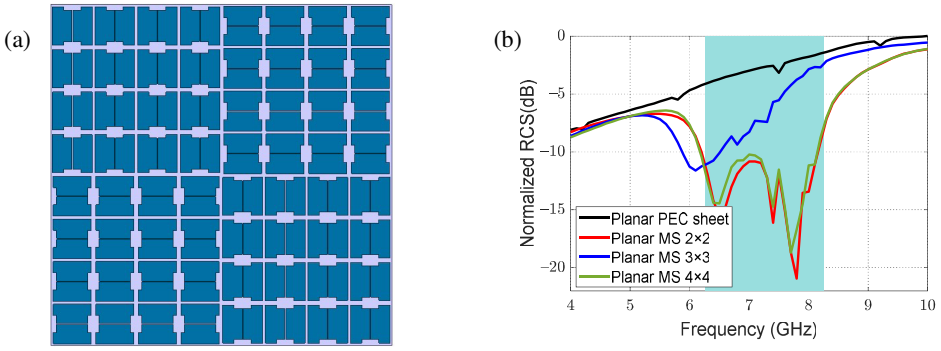

FIGURE 20. (a) Schematic of planner 2×2 chessboard reflecting metasurface. (b) Simulated normalized monostatic RCS for 3 planar Ms sheets compared to perfect conductor sheet of same size: 2×2, 3×3 and 4×4 boards.

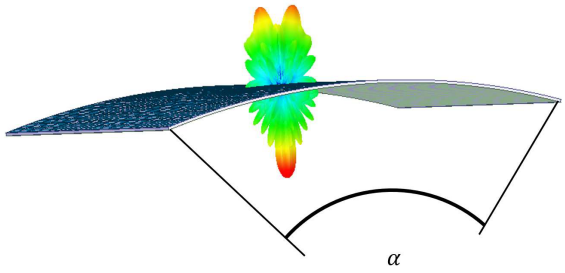

FIGURE 21. Schematic of the 4×4 chessboard Conformal metasurface with bending radius α= 400 mm with plot of the scatted pattern at 6.5 GHz.

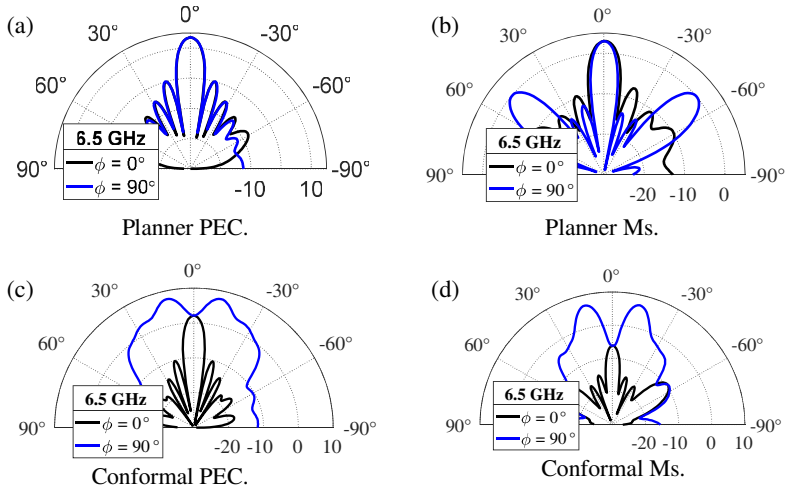

FIGURE 22. Monostatic scattering patterns of conformal metasurfaces at 6.5 GHz using 4×4 array compared to a planner surface applied to a copper cylinder of radius $\alpha = 400$ mm with normal incidence $\theta_i = 0°$. (a) Planner PEC. (b) Planner Ms. (c) Conformal PEC. (d) Conformal Ms.

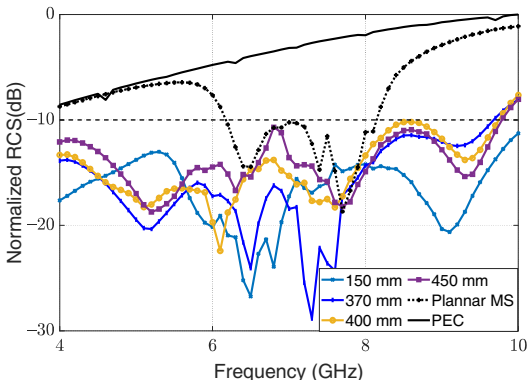

FIGURE 23. Normalized monostatic RCS of 4×4 conformal metasurface at 6.5 GHz of multiple radii compared to PEC sheet of same size as reference.

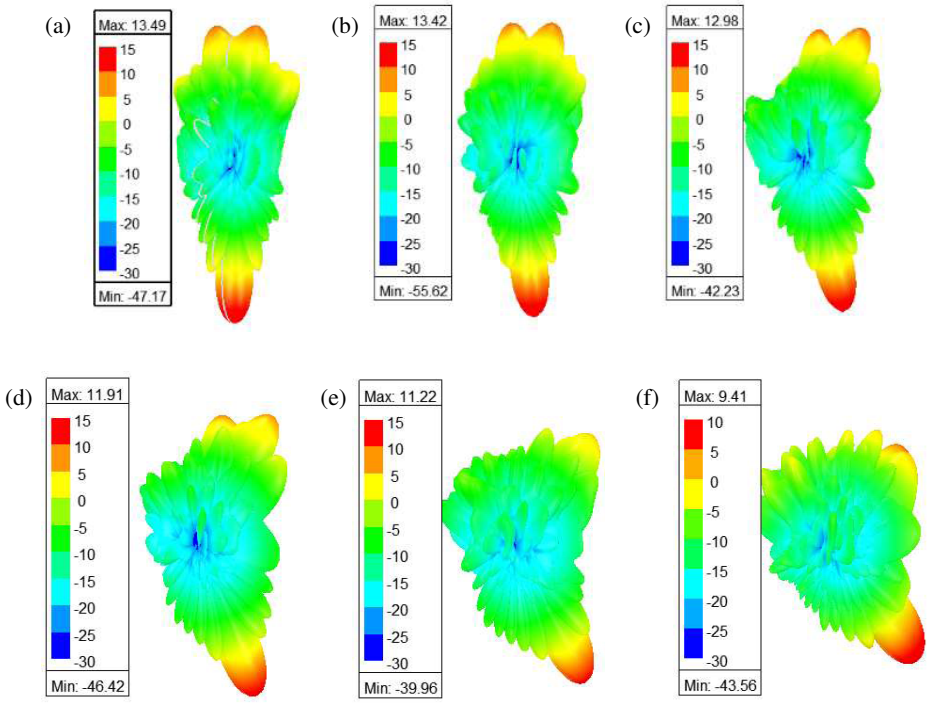

FIGURE 24. Bistatic RCS patterns of 4×4 conformal metasurface at 6.5 GHz of radius $\alpha = 400$ mm with multiple incidence angles. (a) 0°. (b) 10°. (c) 20°. (d) 30°. (e) 40°. (f) 50°.

duction at the same angle. Finally, the field distribution analysis reveals that for the y-polarized incident wave, arrays #2 and #4 (aligned along the y-axis) are predominantly excited near the x-directed edges, as illustrated in Fig. 25. Conversely, under x-polarized wave excitation, arrays #1 and #3 (oriented along the x-axis) exhibit strong excitation primarily at the y-directed edges.

6. MEASURMENTS RESULTS

To verify the accuracy of the simulation and analysis, an MS using arrays was fabricated and tested. The fabricated prototype is depicted in Fig. 26. The figure shows an array consisting of a 2×2 rotated MS, each consists of 4×4 metasurface unit cells 15 mm separated and arranged in 2-D lattice. Fig. 27(a) is the flat model whereas Fig. 27(b) is a conformal design. The designed array is printed on a low loss commercially available grounded substrate, 1.575 mm thick, of ROGERS 5880 (dielectric constant $\epsilon r = 2.2$, loss tangent $\tan\delta = 0.007$). The scattering behavior of the fabricated model was evaluated using the experimental setup shown in Fig. 27. The measurement setup consists of Agilent EXA signal analyzer N9010A, and Agilent E8267D signal generator (SG). For testing for the scattering, the fabricated model was positioned on a platform in front of two identical wideband horn antennas, A-INFO LB-180400-15 operating in the frequency band from 1 GHz to 18 GHz. One of the antennas was connected to a signal generator, while the other was connected to signal analyzer, functioning as the transmitter and receiver, respectively. In order to evaluate the RCS according to the formula in [8], the two orthogonal reflections from the surface should be measured. Two measurement setups were used depicted in Fig. 27(a) and Fig. 27(b) for mea-

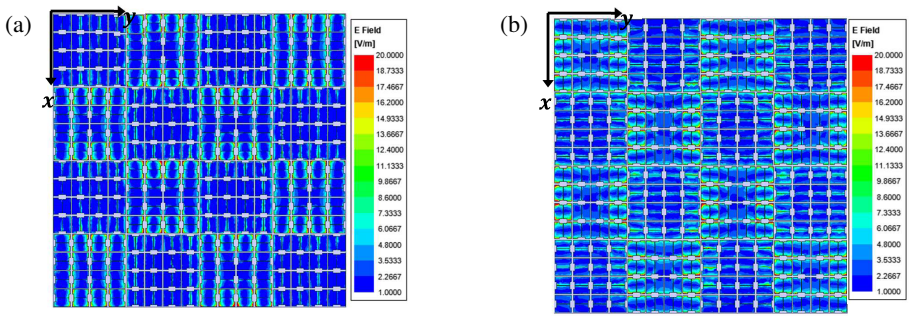

FIGURE 25. E-field distributions at 6.5 GHz. (a) Under y-pol incident wave, (b) Under x-pol incident wave.

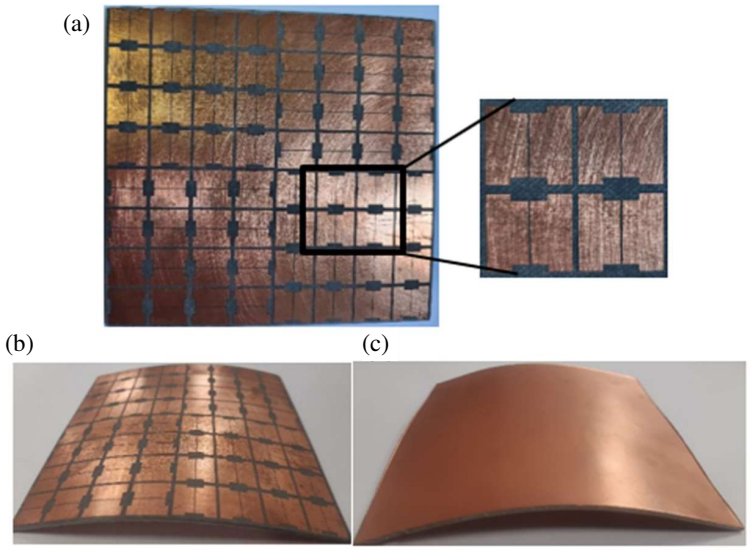

FIGURE 26. The fabricated prototype of 2 × 2MS array. (a) Flat. (b) Conformal. (c) Conformal copper sheet.

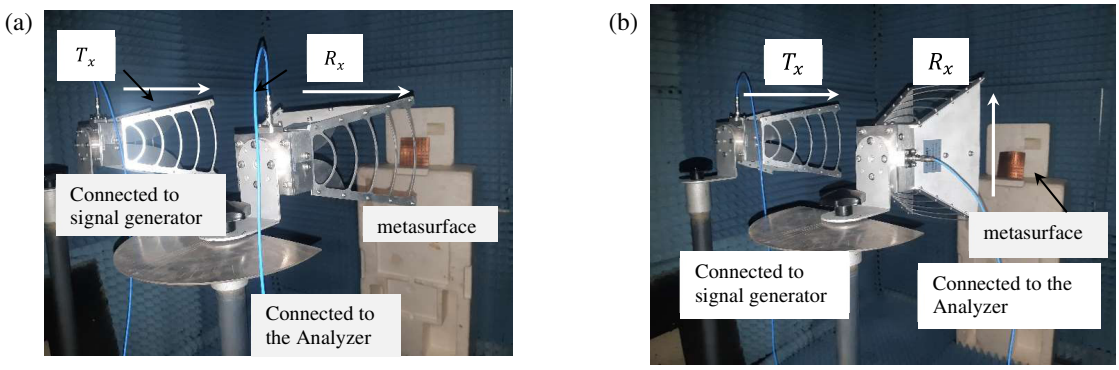

FIGURE 27. Measurement setup for the evaluation of the reflection components. (a) The co-polar component. (b) The cross-polar component.

suring the co-polar and cross-polar components, respectively. In the first setup, the transmitting and receiving horn antennas are oriented in the same direction (x-direction), whereas in the second setup, the receiving horn antenna is y-oriented with keeping the transmitting antenna in the x-direction. The achieved (E_{rx}, φ_{rx}) and (E_{ry}, φ_{ry}) which are the variation of magnitudes and corresponding phases of the two orthogonally reflected waves with frequency are measured. It is worth noting that due to limitations of the used measurement equipment and the availability of only scalar network analyzer, the results achieved reflects the measured reflection magnitudes. Fig. 28 shows the normalized measured reflection magnitude for 5 models, flat copper surface, curved copper surface, flat metasurface, and two curved metasurface sheets with different bends. The results show that generally the MS sheet reduces the RCS; however, the two curved metasurface sheet structures provide the greatest RCS reduction over the 6.3 to 8.3 GHz frequency band.

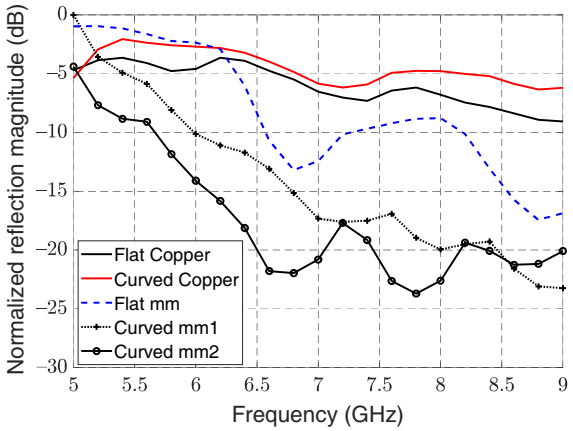

FIGURE 28. Measured monostatic RCS for a normal incidence plane wave for 2 × 2 planar and conformal boards MS sheet compared to perfect conductor sheet of the same size.

7. CONCLUSION

This paper presents a novel wideband conformal metasurface design for radar cross section (RCS) reduction within the 6.3–8.3 GHz frequency range. The proposed metasurface consists of passive unit cells, optimized for integration on curved metallic surfaces. A systematic design methodology is introduced, including the evolution of the unit cell and its application in forming a conformal metasurface array. When being applied to 3D metallic objects, the metasurface effectively generates diffuse scattering patterns and broad scattering angles, regardless of the polarization or incidence angle — achieving more than 10 dB RCS reduction under both monostatic and bistatic configurations across a wide range of incident angles (up to 60°). Both simulated and experimental results confirm the metasurface's ability to suppress specular reflections and enhance stealth characteristics. The proposed design offers a practical and efficient solution for RCS reduction in complex, curved geometries, with strong potential for applications in advanced defense and aerospace stealth technologies. The accuracy of the simulation and analysis was validated through the fabrication and experimental testing of an MS array prototype. The measured results demonstrated that the two curved metasurface sheet structures achieved the most significant RCS reduction within the 6.3 to 8.3 GHz frequency band. RCS performance was evaluated for both conformal surfaces with and without the metasurface attached. The findings confirm that when the proposed design is applied to a metallic object — under normal or oblique incidence angles up to 60° — it consistently achieves more than 10 dB reduction in both monostatic and bistatic RCSs across the specified frequency range. These results verify the effectiveness of the curved metasurface design in practical stealth applications.

REFERENCES

[1] Sun, L., M. Guo, Y. Tong, Z. Hu, P. Huang, X. Zhang, and W. Wang, "Broadband low radar cross section frequency selective surface radome based on phase cancellation and spatial filtering," *Microwave and Optical Technology Letters*, Vol. 66, No. 10, e34334, 2024.

[2] Dhabal, B., A. Kumar, A. Nandi, and B. Basu, "Metamaterial-based AMC antenna with reduced RCS and increased bandwidth for wireless X-band applications," *International Journal of Communication Systems*, Vol. 38, No. 5, e70019, 2025.

[3] Luadang, B., C. Ainthachot, P. Janpangngern, K. Pookkapund, D. Torrungrueng, M. Krairiksh, and C. Phongcharoenpanich, "EBG-backed ultrawideband circularly polarized Archimedean spiral antenna scheme for IoT applications," *Scientific Reports*, Vol. 15, No. 1, 11769, 2025.

[4] Lee, H. and D.-H. Kwon, "Microwave metasurface cloaking for freestanding objects," *Physical Review Applied*, Vol. 17, No. 5, 054012, 2022.

[5] Liu, Q., D. Liang, X. Yao, H. Chen, Q. He, F. Li, L. Zhang, T. Han, L. Yin, and J. Xie, "Broadband RCS reduction metasurface based on vortex singularities generated by spin-to-orbital angular momentum conversion," *Results in Physics*, Vol. 59, 107530, 2024.

[6] Elineau, M., R. Loison, S. Méric, R. Gillard, P. Pagani, G. Mazé-Merceur, and P. Pouliguen, "RCS prediction and optimization for anomalous reflection metasurfaces using Floquet analysis," *International Journal of Microwave and Wireless Technologies*, Vol. 15, No. 6, 966–974, 2023.

[7] Zamel, H. M., E. M. Eldesouki, and A. M. Attiya, "Polarization dependent anomalous reflecting metasurface," *Optical and Quantum Electronics*, Vol. 57, No. 5, 297, 2025.

[8] Zamel, H. M., E. M. Eldesouki, and A. M. Attiya, "Design of anomalous reflecting metasurface for communication systems," *Scientific Reports*, Vol. 15, No. 1, 619, 2025.

[9] Jin, R.-H., Z.-G. Yan, Y.-W. Liu, W.-Z. Lu, and X.-C. Wang, "Wideband function reconfigurable metamaterial for RCS reduction," *IEEE Transactions on Antennas and Propagation*, Vol. 71, No. 11, 9089–9094, 2023.

[10] Narayan, S. and A. Kesavan, *Handbook of Metamaterial-Derived Frequency Selective Surfaces*, Springer Nature, 2023.

[11] Joy, V., A. Dileep, P. V. Abhilash, R. U. Nair, and H. Singh, "Metasurfaces for stealth applications: A comprehensive review," *Journal of Electronic Materials*, Vol. 50, No. 6, 3129–3148, 2021.

[12] Liu, Y., Y. Jia, and S. Gong, *Antenna Radar Cross Section: Theory and Design*, Springer, 2025.

[13] Lin, B., W. Huang, L. Lv, J. Guo, Z. Liu, and R. Zhu, "An ultra-wideband circular polarization-maintaining metasurface and its application in RCS reduction," *IEEE Access*, Vol. 9, 103 967–103 974, 2021.

[14] Soliman, S. A. M., E. M. El-Desouki, S. M. El-Nady, and A. S. A. El-Hameed, "Broadband low RCS based on polarization-dependent artificial magnetic conductor metasurface," *IEEE Access*, Vol. 11, 53 176–53 184, 2023.

[15] Rangula, M. G., P. Paul, B. Majumder, and K. Kandasamy, "An ultra-broadband low profile modified chessboard metasurface with improved backscattering reduction," *Optics Communications*, Vol. 574, 131213, 2025.

[16] Wang, Y., J. Su, Z. Li, Q. Guo, and J. Song, "A prismatic conformal metasurface for radar cross-sectional reduction," *IEEE Antennas and Wireless Propagation Letters*, Vol. 19, No. 4, 631–635, 2020.

[17] Chatterjee, J., A. Mohan, and V. Dixit, "Ultrawideband RCS reduction of planar and conformal surfaces using ultrathin polarization conversion metasurface," *IEEE Access*, Vol. 10, 36 563–36 575, 2022.

[18] Tiwari, P., S. K. Pathak, and V. Siju, "Design, development and characterization of resistive arm based planar and confor-

mal metasurfaces for RCS reduction," *Scientific Reports*, Vol. 12, No. 1, 14992, 2022.

[19] Khan, H. A., A. Majeed, H. Zahra, F. G. Kakepoto, S. M. Abbas, and M. Alathbah, "Transparent conformal metasurface absorber for ultrawideband radar cross section reduction," *Journal of Physics D: Applied Physics*, Vol. 57, No. 13, 135105, 2024.

[20] Yu, N., P. Genevet, M. A. Kats, F. Aieta, J.-P. Tetienne, F. Capasso, and Z. Gaburro, "Light propagation with phase discontinuities: Generalized laws of reflection and refraction," *Science*, Vol. 334, No. 6054, 333–337, 2011.

[21] Zhang, W., Y. Liu, S. Gong, J. Wang, and Y. Jiang, "Wideband RCS reduction of a slot array antenna using phase gradient metasurface," *IEEE Antennas and Wireless Propagation Letters*, Vol. 17, No. 12, 2193–2197, 2018.

[22] Lin, B.-Q., W.-Z. Huang, J.-X. Guo, Y.-W. Wang, B.-G. Huang, and R. Zhu, "Ultra-wideband RCS reduction achieved by a coding phase gradient metasurface," *Plasmonics*, Vol. 18, No. 4, 1561–1569, 2023.

[23] Lin, B., W. Huang, J. Guo, Z. Wang, B. Huang, and K. Si, "An ultra-wideband coding phase gradient metasurface for RCS reduction," *Electromagnetics*, Vol. 43, No. 7, 465–476, 2023.

[24] Lin, B., W. Huang, J. Guo, B. Huang, Y. Wang, R. Zhu, and Z. Wang, "An ultra-wideband phase gradient metasurface for anomalous reflection and RCS reduction," *Optics Communications*, Vol. 545, 129704, 2023.

[25] Ullah, M. U., T. B. A. Latef, M. Othman, M. I. Hussein, H. M. Alkhoori, Y. Yamada, K. Kamardin, and R. Khalid, "A progression in the techniques of reducing RCS for the targets," *Alexandria Engineering Journal*, Vol. 100, 153–169, 2024.

[26] Dong, G., S. Zhu, Y. He, S. Xia, A. Zhang, X. Wei, and Z. Xu, "Radar cross section reduction metasurface based on random phase gradients," *Applied Physics B*, Vol. 124, No. 11, 222, 2018.

[27] Sarkar, S. and B. Gupta, "Artificial magnetic conductor with self-complementary unit cells having very high angular stability," *Electronics Letters*, Vol. 56, No. 14, 704–706, 2020.

[28] Mondal, A., R. Bose, S. Pal, A. Kundu, and S. Sarkar, "A polarization independent artificial magnetic conductor with wide reflection phase bandwidth and good angular stability," in *2024 IEEE Calcutta Conference (CALCON)*, 1–4, Kolkata, India, 2024.

[29] Fu, C., L. Han, C. Liu, Z. Sun, and X. Lu, "Dual-band polarization conversion metasurface for RCS reduction," *IEEE Transactions on Antennas and Propagation*, Vol. 69, No. 5, 3044–3049, 2021.

[30] Tiwari, P., S. K. Pathak, and V. Siju, "Development of resistive-ink based planar and conformal metasurfaces for RCS reduction," *IEEE Access*, Vol. 10, 61 472–61 483, 2022.

[31] Fu, C., L. Zhang, L. Liu, S. Dong, W. Yu, and L. Han, "RCS reduction on patterned graphene-based transparent flexible metasurface absorber," *IEEE Transactions on Antennas and Propagation*, Vol. 71, No. 2, 2005–2010, 2023.

[32] Wang, J., Q. Zhao, F. Fu, K. Wang, Z. Ye, S. Yin, H. Wang, and L. Wang, "Optimization of wideband RCS reduction via controlled phase and amplitude in metasurface design," *Applied Physics A*, Vol. 130, No. 4, 220, 2024.